RSC Advances

PAPER

View Article Online
View Journal | View Issue

Cite this: *RSC Adv.*, 2026, **16**, 6288

Excited-state intramolecular charge transfer dynamics in 4-methoxy-4′-nitrostilbene: excitation wavelength and solvent dependence

Prajoy Kumar Mitra, Shamil R and Yapamanu Adithya Lakshmanna *

We present a detailed study of the excited-state dynamics of 4-methoxy-4′-nitrostilbene (MNS), a donor–acceptor chromophore, focusing on the effects of solvent polarity, viscosity, and excitation energy. Steady-state spectroscopy reveals strong intramolecular charge transfer (ICT) behavior, with solvatochromic shifts and large Stokes shifts in polar solvents. Time-resolved fluorescence measurements show that both polarity and viscosity enhance ICT state stabilization by extending emissive state lifetimes. Femtosecond transient absorption measurements in toluene and acetonitrile reveal distinct spectral features and relaxation dynamics upon excitation at different wavelengths. In the case of toluene, 370 and 310 nm excitations lead to efficient intersystem crossing (ISC) as depicted by a strong and persistent excited state absorption (ESA) band at ~600 nm. In case of acetonitrile, ISC is slower, and very weak ESA associated with a triplet state is observed under the same excitations. While in the case of 510 nm excitation, ESA band at 540 nm is stable, and does not exhibit any spectral shift in both the solvents, a clear indication of inefficient ISC and relaxation essentially occurs through a different pathway. The experimental observations are well corroborated with computational analysis carried out using time-dependent density functional theory. These findings highlight tunable excited-state behavior in donor–acceptor systems for photonic applications.

Received 7th November 2025
Accepted 19th January 2026

DOI: 10.1039/d5ra08595k

rsc.li/rsc-advances

Introduction

Understanding the excited-state dynamics of chromophores with intramolecular charge transfer (ICT) character is essential for advancing their applications in optoelectronics, fluorescence imaging, solar energy harvesting, and nonlinear optics (NLO).[1–5] Donor–acceptor (D–A) systems, especially those featuring π-conjugated linkers, are of particular interest due to their tunable electronic properties, which are highly responsive to solvent polarity, molecular conformation, and excitation conditions.[6–11] These systems often exhibit solvatochromic behavior, enhanced dipole moments in the excited state, and complex relaxation pathways that include twisting, internal conversion, and intersystem crossing (ISC).[12–16]

Stilbene derivatives represent a well-known class of π-conjugated molecules that exhibit diverse photoinduced properties, including isomerization, twisted ICT (TICT) formation, and fluorescence modulation.[17–32] Their structural simplicity, combined with responsive excited-state properties, has made them model systems for probing solvent effects and conformational dynamics, especially in D–A frameworks such as push–pull nitrostilbenes. In these push–pull molecules, light absorption leads to the formation of intramolecular charge-transfer (CT) states whose relaxation behaviors are strongly governed by both solvent polarity and viscosity. Experimental evidence shows that solvent polarity can drastically alter the efficiency of excited-state processes, influencing pathways such as torsional relaxation, TICT state generation, and ISC to triplet states followed by subsequent isomerization.[33–44] For donor-substituted nitrostilbenes like *trans*-4-(*N*, *N*′-dimethylamino)-4′-nitrostilbene (DMANS), pronounced solvent-dependent fluorescence is observed, with efficient emission in non-polar environments but strong quenching in polar media.[33] In sharp contrast, the unsubstituted counterpart, *trans*-4-nitrostilbene (t-NSB), exhibits minimal fluorescence across solvents, reflecting the predominance of ISC and subsequent triplet-driven photoisomerization, both largely insensitive to solvent polarity.[19,28–30] This discrepancy highlights the important role of strong CT character in suppressing ISC and enhancing radiative decay, a feature absent in t-NSB. Moreover, excitation wavelength has emerged as a key factor in controlling singlet–triplet branching, particularly in heavy-atom-free systems where ISC relies on favorable energy gaps and spin–orbit coupling (SOC). Selective excitation can directly affect ISC rates and influence the distribution between singlet and triplet states, illustrating subtle ways to tailor photophysical behavior in all-organic chromophores.[45–54]

In this context, 4-methoxy-4′-nitrostilbene (MNS) represents a classic donor–acceptor chromophore featuring a methoxy

School of Chemistry, Indian Institute of Science Education and Research, Vithura, Thiruvananthapuram 695551, India. E-mail: adithya@iisertvm.ac.in

donor and nitro acceptor across a stilbene bridge. Its conjugated push–pull structure facilitates ICT and solvatochromic behaviour.[55] However, its detailed excited-state relaxation dynamics remain largely unexplored. Key factors such as solvent polarity, viscosity, and excitation energy may significantly influence ICT-state stabilization, fluorescence lifetime, and triplet-state formation. A deeper understanding of how these factors impact fluorescence lifetimes, ICT stabilization, and potential triplet formation in MNS could offer broader insights into the behaviour of classic D–A systems in diverse optical environments.

In this study, we present a comprehensive investigation of MNS using steady-state absorption and emission spectroscopy, femtosecond fluorescence upconversion, and femtosecond transient absorption (fs-TA) spectroscopy. By probing MNS in solvents ranging from non-polar to polar and in viscous media, including long-chain alcohols and polyethylene glycol 300 (PEG 300), we uncover how the environment modulates ICT process, fluorescence lifetime, and ISC efficiency. Excitation-wavelength-dependent fs-TA studies (excitations at 370, 310, and 510 nm) in toluene and acetonitrile reveal distinct relaxation pathways and triplet state formation behaviour. In addition to this, a complementary time-dependent density functional theory (TDDFT) and natural transition orbital (NTO) analyses confirm the ICT character of the S_1 state and availability of energetically accessible triplet states. SOC calculations highlight efficient ISC pathways, while computed polarizability and hyperpolarizability values further reflect solvent-induced stabilization of the ICT state. Together, these results provide mechanistic insight into excited-state relaxation in MNS and underscore the continued relevance of classic D–A scaffolds for photonic and nonlinear optical applications.

Material and methods

Sample preparation

4-Methoxy-4′-nitrostilbene (MNS) was purchased from TCI (>98% purity) and was used without any further purification. All the solvents such as toluene (TOL), 1,4-dioxane (DOX), ethyl acetate (EA), acetonitrile (MeCN), methanol (MeOH), isopropanol (PrOH), butanol (BuOH), pentanol (PnOH), and PEG 300, used in the experiments were of HPLC grade from Spectrochem and used without further purification.

Steady-state spectroscopic measurements

Steady-state absorption spectra were recorded using a Shimadzu UV-3600 UV-vis–NIR spectrophotometer, and fluorescence emission measurements were carried out on a Horiba Jobin Yvon Fluorolog-3 spectrofluorometer. All measurements were conducted in a standard 1 cm path length quartz cuvette. The molecular structure of the MNS is shown in Chart 1.

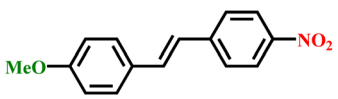

Chart 1 Molecular structure of MNS.

Femtosecond transient absorption (fs-TA) measurements

Femtosecond transient absorption (fs-TA) measurements were carried out using a home-built setup. Briefly, the setup consists of a Ti: sapphire amplifier system (Spectra Physics) operating at a central wavelength of 800 nm, with a pulse duration of 100 fs, pulse energy of ~5 mJ, and a repetition rate of 1 kHz. The laser output was divided into two parts: one portion was directed to an optical parametric amplifier (OPA) to generate pump pulses at 310, 370, and 510 nm (100 fs, 10 μJ, 1 kHz), while a small fraction of the remaining beam was used to produce a white-light continuum by focusing into a CaF_2 plate. The whitelight continuum was then split into probe and reference beams. The pump and probe pulses were spatiotemporally overlapped in a 1.0 mm path length cell containing the sample. The probe beam was dispersed by a spectrometer and detected with a dual-array detector. Pump modulation was achieved using a mechanical chopper at 500 Hz to isolate the excited-state signal at each delay time. Transient absorption experiments were conducted with a pump energy of 120 nJ (for 310 nm and 370 nm) and 200 nJ (for 510 nm) with a focal spot diameter of approximately 100 μm on the sample. A 0.5 mM solution of MNS was used for both fs-TA and fluorescence upconversion measurements.

Femtosecond fluorescence upconversion measurements

Femtosecond fluorescence upconversion measurements were performed using a FOG-100 setup (CDP Systems). The sample was excited at 400 nm, generated *via* second harmonic generation of the fundamental beam from a Mai Tai HP laser (central wavelength of ~800 nm, pulse duration of ~100 fs, and repetition rate of 80 MHz). The emitted fluorescence and residual fundamental beam were spatially overlapped in a nonlinear beta barium borate (BBO) crystal to produce a sum-frequency signal, yielding an upconverted fluorescence. Such signal was then directed through a double monochromator and detected using a sensitive photomultiplier tube coupled with a photon counting system. Fluorescence upconversion decay profiles were analysed using an in-house prepared code based on iterative multi-exponential analysis. All steady-state measurements, fs-TA, and fluorescence upconversion measurements were carried out at room temperature (295 K).

Computational methodology

All computations were carried out using the Gaussian 16 software package.[56] Geometry optimizations were performed at the CAM-B3LYP/6-311 + G(d,p) level of theory, incorporating solvent effects for TOL and MeCN using the integral equation formalism polarizable continuum model (IEFPCM). Vertical excitation energies and NTOs were calculated using TDDFT. SOC constants were computed using the ORCA 6.0.0 program package based on the optimized geometries.[57] Additionally, static polarizability (α), and first hyperpolarizability (β) values

were evaluated to probe the molecule's nonlinear optical (NLO) response.

Results and discussion

Steady-state measurements

Steady-state absorption and emission measurements were performed in non-polar and polar environments, including TOL, DOX, EA, and MeCN. The absorption spectra, as shown in Fig. 1, remained nearly identical across all the solvents, indicating that the ground-state electronic structure of MNS is largely unaffected by solvent polarity. However, the emission spectra showed a pronounced red-shift with increasing solvent polarity. The emission maximum appears at 470 nm in the non-polar solvent TOL, at 500 nm in low-polarity DOX, at 540 nm in medium-polarity EA, and at 630 nm in highly polar MeCN. Such substantial solvatochromic shift suggests the stabilization of an ICT excited state in polar media. The absorption and emission spectral parameters are summarized in Table 1.

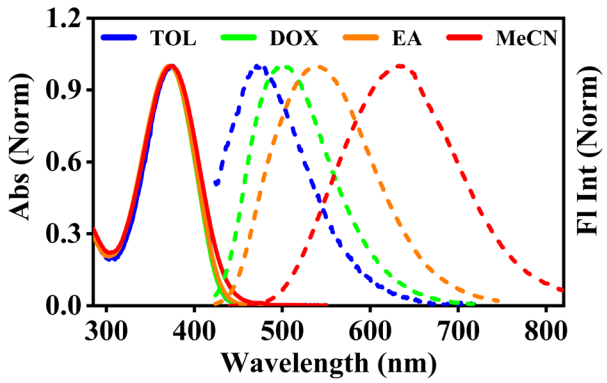

Fig. 1 The steady-state absorption (solid lines) and emission (dotted lines) spectra of MNS in solvents of varying polarities.

Table 1 Solvent dependent spectral parameters of the absorption and emission spectra that include the solvent's dielectric constant (ε),[58] peak wavelengths of absorption (λ_{abs}) and emission (λ_{fl}), along with the Stokes shift ($\Delta\nu^{-1}$)

Solvent	ε	λ_{abs} (nm)	λ_{fl} (nm)	$\Delta\nu^{-1}$ (cm^{-1})
TOL	2.37	375	470	5390
DOX	2.21	372	500	6880
EA	6.08	372	540	8360
MeCN	36.64	375	630	10 800

The Stokes shift grows from 5390 cm^{-1} in TOL to 10 800 cm^{-1} in MeCN. Additionally, the fluorescence quantum yield (Φ_{fl}) rises with increasing solvent polarity (Table 2), supporting the formation of a stabilized, emissive ICT state. The Φ_{fl} is relatively low in TOL but markedly high in MeCN, suggesting that non-radiative decay pathways are suppressed in polar solvents. This trend aligns with the strong ICT nature of the excited state, whose radiative efficiency is enhanced through solvent stabilization.

Time-resolved fluorescence dynamics

The fluorescence upconversion experiments were performed to investigate the excited-state emissive lifetime of MNS in solvents of varying dielectric constants. The samples were excited at 400 nm, and the fluorescence decay profiles were measured at the respective emission maximum for each solvent, as shown in Fig. 2. The amplitude decay kinetics were best described by a biexponential model, yielding two characteristic time constants (τ_1 and τ_2), that are summarized in Table 2. The reported fluorescence lifetimes and quantum yields represent reproducible values obtained from repeated measurements under identical experimental conditions. The fluorescence lifetimes were obtained from exponential fitting of the time-resolved decays. Relative fluorescence quantum yields were determined using a standard reference method and are associated with an estimated uncertainty of ±5%. The corresponding uncertainties in the radiative (k_r) and non-radiative (k_{nr}) rate constants were calculated by standard propagation of errors from the quantum yields and measured lifetimes.

In TOL, the fast component, $\tau_1 \approx 0.4$ ps is attributed to the ultrafast relaxation of initially prepared state, while the slower component, $\tau_2 \approx 10$ ps corresponds to the fluorescence lifetime of MNS. As solvent polarity increases, a progressive increase in the longer time component is observed, *i.e.*, 29.6 ps in DOX, 199 ps in EA, and a substantial enhancement to 224 ps in the highly polar solvent, MeCN. The increase in fluorescence lifetime with solvent polarity indicates stabilisation of the emissive ICT state. However, enhanced ICT character in polar solvents does not necessarily imply the formation of a fully twisted ICT (TICT) state. The TICT state is typically associated with weak emission due to a reduced or smaller donor–acceptor overlap. In case of MNS, the emissive excited state is therefore likely to retain a planar geometry with sufficient donor–acceptor orbital

Table 2 Kinetic parameters associated with the emission spectrum of MNS in different solvents. The parameters include the fluorescence quantum yield (Φ_{fl}), fluorescence lifetimes (τ_1 and τ_2), and the rate constants for radiative (k_r) and non-radiative (k_{nr}) decay processes across solvents of varying polarity. τ_1 and τ_2 were obtained from decay fitting, while relative Φ_{fl} carry an estimated uncertainty of ±5%. Uncertainties in k_r and k_{nr} were calculated by standard error propagation from Φ_{fl} and the measured lifetimes

Solvent	Φ_{fl} (10^{-2})	τ_1 (ps)	τ_2 (ps)	k_r (10^8 s^{-1})	k_{nr} (10^{10} s^{-1})
TOL	1.5 ± 0.08	0.39 ± 0.02	9.6 ± 0.3	15.6 ± 0.96	10.3 ± 0.32
DOX	1.7 ± 0.09	0.78 ± 0.03	29.6 ± 0.3	5.74 ± 0.31	3.32 ± 0.03
EA	3.4 ± 0.17	33.6 ± 1.9	199 ± 13.1	1.71 ± 0.14	0.48 ± 0.03
MeCN	9.9 ± 0.50	22.8 ± 0.7	224 ± 7.5	4.42 ± 0.27	0.40 ± 0.01

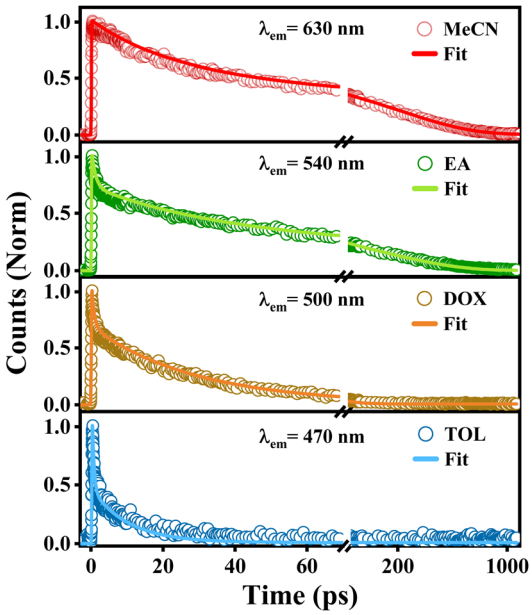

Fig. 2 The fs-Fluorescence upconversion decay profiles of MNS measured at the emission maxima in solvents with different polarities. Solid lines indicate the fitted curves.

overlap to support radiative decay, consistent with the TD-DFT results.

The solvent dependence of the radiative and non-radiative rate constants further suggests that non-radiative relaxation is strongly influenced by large-amplitude torsional motions rather than by the energy gap law alone. Increased stabilisation of the ICT minimum in polar environments can restrict access to these torsional relaxation pathways, leading to reduced k_{nr} despite a smaller S_1–S_0 energy gap. Importantly, this stabilisation does not directly enhance the radiative rate constant but instead suppresses competing non-radiative channels, rendering radiative decay comparatively more favourable.

Femtosecond transient absorption measurements

To investigate how excitation into different electronic states affects the subsequent excited-state evolution of MNS, we performed fs-TA measurements at three distinct excitation wavelengths: 310 nm, 370 nm, and 510 nm. These experiments were carried out in two solvents of contrasting polarity, TOL and MeCN. The selection of excitation wavelengths was essentially guided by both absorption and TDDFT calculations (detailed discussion is given in a later section), which indicate that excitation at 310 nm accesses higher-lying excited configurations energetically corresponding to the S_2 region, 370 nm primarily populates the lowest singlet state S_1, and 510 nm, a wavelength which is away from the absorption band that accesses higher singlet states such as S_6 through multi-photon absorption.

In non-polar environment. In case of TOL, excitation at 370 nm promotes MNS directly to the first singlet excited state (S_1), resulting in an intense positive excited-state absorption (ESA) band centered around 570 nm. The fs-TA spectra at different time delays are shown in Fig. 3b. At initial time delays, the ESA maximum exhibits a red-shift, accompanied by a gradual decrease in intensity near 600 nm, and ultimately stabilizes. The ESA band persists for long time delays beyond 3 ns. Upon global analysis of the fs-TA data, the data was best fit with tri-exponential model, with a fast component, $\tau_1 \sim 0.5$ ps attributed to ultrafast relaxation, followed by a second time component, $\tau_2 \sim 6.4$ ps, which is assigned to the time scale of ISC from S_1 to a lower-lying triplet state. The third time component is attributed to the lifetime of the triplet state. The ESA band subsequently settles into a persistent long-lived feature, characteristic of triplet state absorption. In case of 310 nm excitation, the fs-TA spectra for different time-delays are shown in Fig. 3a. Such excitation essentially populates higher-lying excited configurations in the S_2 energy region, leading to broader ESA feature at early time delay. Based on TD-DFT calculations in the following section, this excitation does not selectively populate an S_2 state but rapidly relaxes to the lowest singlet excited state *via* internal conversion. The fs-TA features eventually evolve into the features as observed under 370 nm excitation. The amplitude decay proceeds *via* rapid IC with a timescale of ~0.2 ps to S_1, followed by ISC with at time constant of ~7.6 ps to the triplet state. Despite the differences in the initial spectral features, the molecule eventually relaxes to the similar long-lived triplet state, confirming a common final excited state regardless of the excitation energy. To further verify this, excitation spectra were recorded and found to closely overlap with the corresponding absorption spectra (Fig. S3), confirming that emission originates from the same emissive state following excitation at both wavelengths. The similarity of the fs-TA dynamics therefore reflects rapid internal conversion from initially accessed higher-lying excited configurations to the lowest singlet excited state (S_1), rather than selective population of a distinct S_2 state. While in case of 510 nm excitation, the ESA exhibits the following features: amplitude is weaker as compared to the 310 nm and 370 nm excitations, band is centered at ~540 nm with no observable red-shift over time, and no sign of band appearance near 600 nm in contrast to the dynamics observed at 370 and 310 nm. These features suggest that MNS is likely to follow a different excited-state relaxation pathway upon 510 nm excitation due to the two-photon absorption or weak direct excitation to a distinct high-energy singlet state. In fs-TA measurements, the recorded ΔA reflects the net effect of contribution from ground-state bleach (GSB), stimulated emission (SE), and ESA. For excitation at 310 and 370 nm, the absence of distinct negative ΔA features in the region below 540 nm in Fig. 3 indicates that SE from the emissive ICT state is weak (1.5% of Φ_{fl}) and overlaps with ESA from the S_1 state, leading to an overall positive ΔA. In contrast, excitation at 510 nm occurs in a spectral region with negligible one-photon absorption and therefore proceeds *via* multiphoton excitation, leading to transient spectra dominated by ESA rather than SE. The global analysis of the fs-TA data reveals the best fit with tri-exponential model with $\tau_1 = 0.9$ ps, $\tau_2 = 16.4$ ps, and τ_3 = long lived (>3 ns). Interestingly, the spectral features do not exhibit any shift with time and persist for the time delays above 3 ns. Furthermore, the ESA band does not contain the band

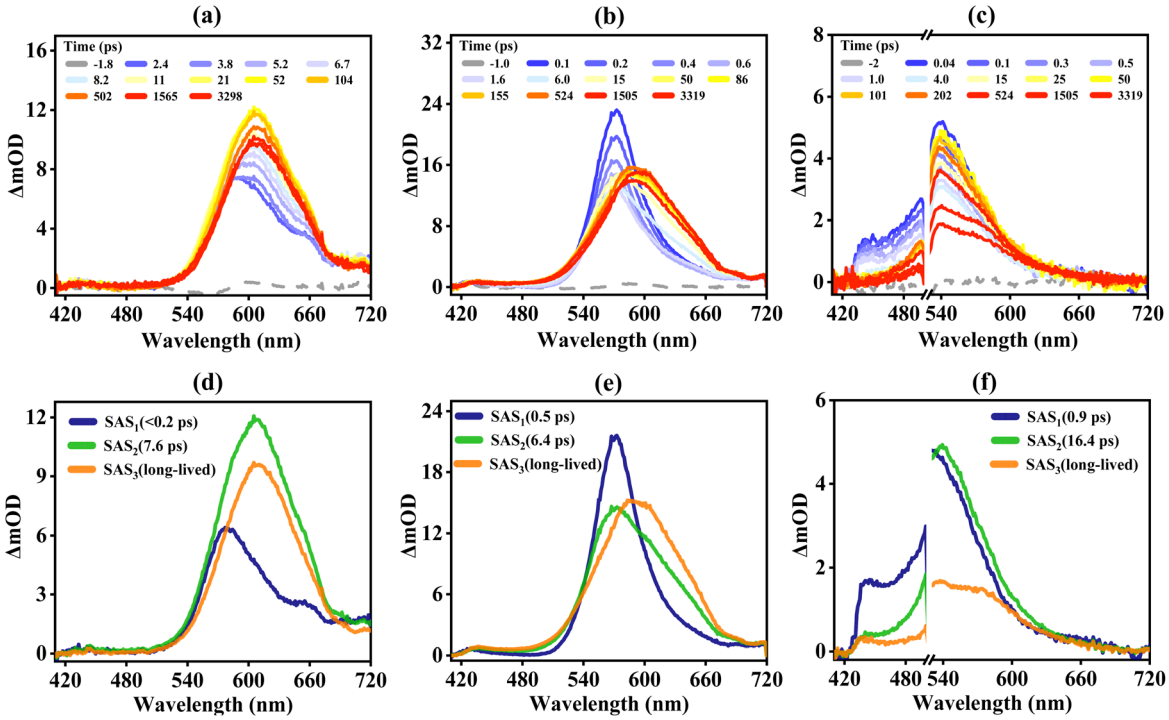

Fig. 3 The fs-TA spectra of MNS in TOL at different time delays while exciting with (a) 310 nm, (b) 370 nm, and (c) 510 nm. Species-associated spectra of fs-TA for excitations at (d) 310 nm, (e) 370 nm, and (f) 510 nm.

around ~600 nm (as observed in 310 nm and 370 nm excitations). These spectral features clearly depict that MNS, upon 510 nm excitation, most likely evolves through distinct states as compared to the excitations at 310 nm and 370 nm.

In polar environment. In case of MNS in MeCN, upon excitation at 370 nm, the fs-TA as shown in Fig. 4b exhibits a positive ESA band centered around 540 nm, and a broad negative band centered around 620 nm. The excitation at 370 nm is associated with transition to the S_1 state. The negative band feature in the fs-TA spectrum is considered as SE band as it matches well with the steady-state emission spectrum. As the excited-state relaxation progresses, both the SE and the ESA

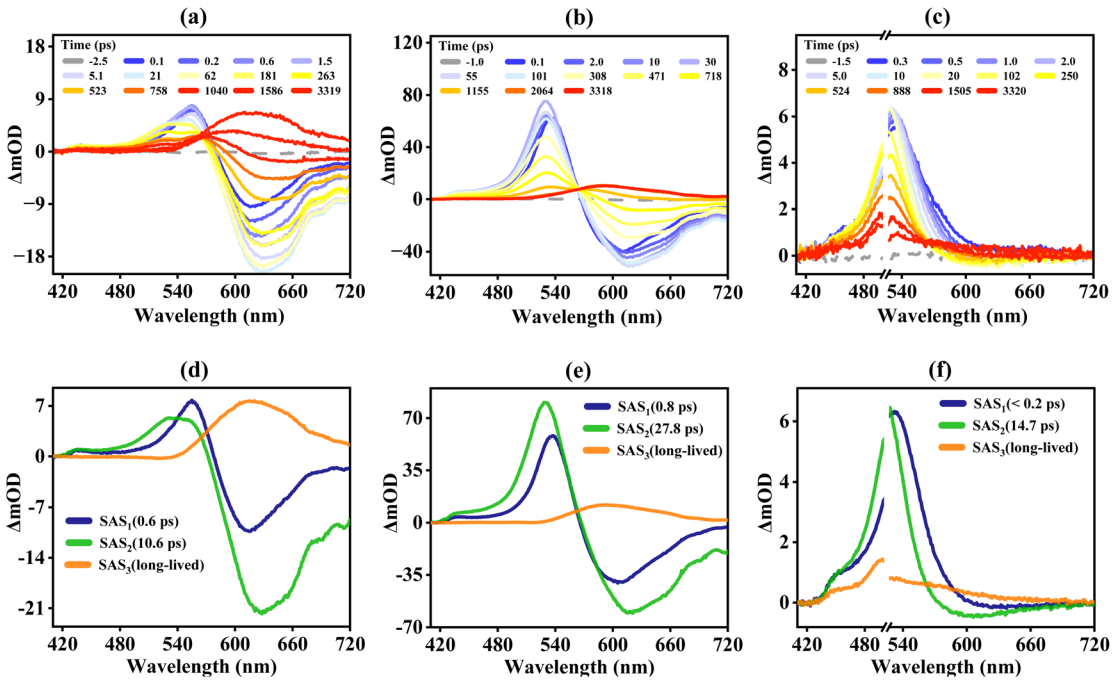

Fig. 4 The fs-TA spectra of MNS in MeCN for different time delays while exciting at (a) 310 nm, (b) 370 nm (c) 510 nm. Species-associated spectra of fs-TA data for excitations at (d) 310 nm, (e) 370 nm, and (f) 510 nm.

bands gradually diminish in their amplitudes, while a new positive ESA band emerges around 600 nm at longer delay times. The ESA band at 600 nm retains its amplitude for longer time delays, a clear indication of triplet-state absorption. The decay kinetics include a fast ~0.8 ps component, attributed to vibrational relaxation, and a slower ~27.8 ps component, associated with ISC. Notably, ISC is slower in MeCN than in TOL, likely due to solvent stabilization of the S_1 state, which reduces the efficiency of ISC. A similar solvent-dependent slowing of ISC due to S_1 stabilization has been reported for *trans*-4-nitrostilbene in ultrafast transient absorption studies.[28]

In case of excitation at 310 nm, the fs-TA spectra as shown in Fig. 4a exhibits a positive broad ESA band centered near 540 nm and a SE band beyond 600 nm. The ESA and SE bands gradually decrease in their amplitudes with time. However, for time delays above 1 ns, the fs-TA exhibits a predominantly positive band around 600 nm. The fs-TA spectra were best fit globally with tri-exponential model with time constants of $\tau_1 = 0.6$ ps, $\tau_2 = 10.6$ ps, and $\tau_3 =$ long-lived (>3 ns). The time constants τ_1, τ_2, and τ_3 are attributed to the internal conversion ($S_2 \rightarrow S_1$), ISC and lifetime of long-lived triplet state, respectively. Despite the initial differences, the molecule relaxes to the same triplet state as observed under 370 nm excitation.

In case of excitation at 510 nm, the fs-TA spectra as shown in Fig. 4c exhibits predominantly ESA band centered at 530 nm during the initial time delays. As the time delay increases, appearance of weak negative band around 620 nm is noticed (the amplitude is very weak as compared to SE bands for the cases of other excitations). It is also clear from the Fig. 4c that the shift in the ESA band is minimal, and the band is persistent for long time delays. The fs-TA data was globally best fit with tri-exponential model. The time constants of $\tau_1 = 0.2$ ps, $\tau_2 = 14.7$ ps, and $\tau_3 =$ long-lived (>3 ns) are attributed to internal conversion from higher-lying singlet state, ISC, and long-lived triplet state. This is consistent with ultrafast transient absorption studies on *trans*-4-nitrostilbene, where sub-picosecond dynamics were assigned to internal conversion, tens-of-picosecond components to ISC, and nanosecond-scale signals to triplet-state absorption.[28] Unlike cases of 310 nm and 370 nm excitations, the ESA band remains centered at ~530 nm throughout the observed time window, with no significant rise of a 600 nm band. The lack of spectral evolution around 600 nm implies that the molecule may not access the same triplet state, or the triplet population is minimal in MeCN under 510 nm excitation, likely due to solvent stabilization of singlet states and enhanced non-radiative decay. Further, to gain deeper insight into the excited-state dynamics, we extracted single-wavelength kinetic traces from selected spectral regions of the fs-TA data in both TOL and MeCN. The resulting amplitude-versus-time plots, corresponding to key spectral features, are presented in Fig. S1 and S2, respectively. In TOL, transient absorption monitored at 600 nm following excitation at 310 and 370 nm exhibits an initial rise ($\tau_1 \approx 7.2$ and 6.7 ps, respectively), followed by a long-lived decay. Excitation at 510 nm with observation at 540 nm instead reveals a slower rise of ~15 ps, which likewise evolves into a long-lived regime. These rise time components are attributed to relaxation or population transfer into the observed spectral bands, while the persistent signals are consistent with triplet-state absorption. In MeCN, the early dynamics are markedly faster. At 530 nm, following excitation at 310 or 370 nm, sub-picosecond rises ($\tau_1 = 0.5$ and 0.3 ps) are observed, followed by slower decays of ~548 and 556 ps, respectively. At 620 nm, ultrafast decays (0.5–0.6 ps) precede slower components (9.3–14.5 ps), with additional long-lived rises, reflecting competing decay of singlet states and triplet-state formation. Upon 510 nm excitation, signal monitored at 535 nm shows 13.6 ps decay component that transitions into a long-lived component, while at 610 nm, an ultrafast decay (0.81 ps) is followed by a delayed rise (~1081 ps), indicative of secondary population channels, likely *via* ISC. Overall, the comparison demonstrates that in MeCN, early-time processes such as vibrational relaxation and internal conversion occur more rapidly than in TOL. Furthermore, triplet formation and its subsequent kinetics are strongly influenced by solvent polarity, consistent with stabilization of the S_1 state in polar media and the resultant reduction in ISC efficiency.

It is noticed that excitation of MNS with 370 nm and 310 nm in both the solvents ultimately lead to a common triplet state, although the efficiency and timescale of ISC are different. In case of TOL, the formation of triplet state is associated with faster ISC, efficient, and high amplitude ESA at ~600 nm. Whereas in MeCN, the formation of triplet state is associated with slow ISC, with broad and weak amplitude. However, in case of excitation of MNS with 510 nm in MeCN, triplet formation is inefficient, with no clear spectral evolution, indicating excitation-dependent dynamics in polar media. These results highlight the strong influence of solvent polarity and excitation energy on excited-state relaxation pathways.

The possibility of photoinduced *E*/*Z* isomerisation contributing to the long-lived transient absorption was also considered. In stilbene-based systems, *E*/*Z* isomerisation typically occurs on ultrafast (ps to tens of ps) timescales and is followed by rapid relaxation to the ground state, and therefore does not usually give rise to ESA persisting into the nanosecond regime. In the present case, the ESA band centred around ~600 nm persists throughout the full fs-TA temporal window (up to 3.3 ns) without the appearance of new long-lived ground-state absorption or bleach features indicative of stable photo-product formation. Moreover, the steady-state absorption spectrum of an isolated *Z*-isomer was not recorded, as the *Z*-isomer of MNS was not independently generated or isolated under our experimental conditions. Based on the long lifetime, spectral characteristics, and comparison with literature reports on nitro-substituted stilbene derivatives,[28] the ~600 nm ESA is therefore assigned to triplet–triplet absorption.

Hydrogen-bonding and viscosity effects

To investigate how hydrogen bonding and viscosity influence excited-state relaxation dynamics, a series of polar protic solvents, including MeOH, PrOH, BuOH, and PnOH, were studied. These solvents are associated with a gradual increase in alkyl chain length and viscosity, from 0.54 cP (MeOH) to 4.00 cP (PnOH), while also differing in hydrogen-bonding strengths.

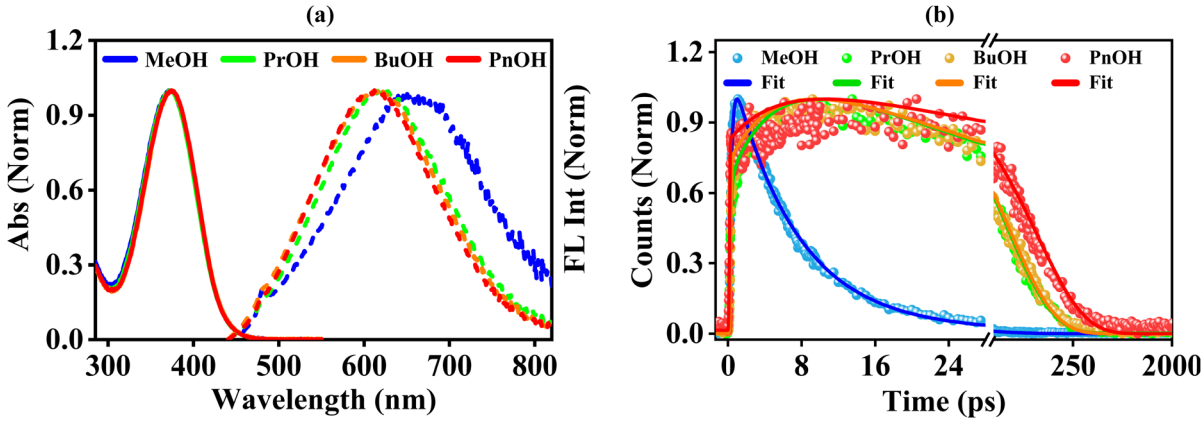

Fig. 5 (a) Steady-state absorption (left), emission (right), and (b) fs-fluorescence up-conversion spectra of MNS in polar protic solvents.

Table 3 Solvent dependent spectral parameters of the absorption and emission spectra that include the solvent's dielectric constant (ε), solvent viscosity η, along with the peak wavelengths of absorption (λ_{abs}) and fluorescence (λ_{fl}).[53] Measurements at 295 K

Solvent	ε	η (cP)	λ_{abs} (nm)	λ_{fl} (nm)
MeOH	33	0.54	372	650
PrOH	20.18	2.03	373	620
BuOH	17.84	2.54	375	615
PnOH	15.13	3.61	375	612

This allows us to assess how solute–solvent interactions and restricted molecular motion modulate the relaxation pathways of the ICT excited state. Steady-state measurements revealed significant solvent-dependent spectral shifts as shown in Fig. 5a. The absorption spectra remain largely unchanged across the alcohol series. However, the emission maxima exhibit a clear trend, with MeOH showing the most red-shifted emission (650 nm), followed by a progressive blue shift in PrOH (620 nm), BuOH (615 nm), and PnOH (612 nm). The red-shifted emission in MeOH likely arises from stronger hydrogen bonding and higher polarity, which stabilizes the emissive ICT state more effectively than the relatively less polar, and longer-chain alcohols (Table 3).

Femtosecond fluorescence up-conversion measurements were carried out at 620 nm in each case, where ICT emission dominates. The corresponding plots are depicted in Fig. 5b. The emission amplitude kinetics were best fit with biexponential model. In case of MeOH, the amplitude decay was characterized by a fast component at $\tau_1 = 0.25$ ps, and a short-lived emissive state at $\tau_2 = 7.2$ ps. These time constants are attributed to due to ultrafast ICT formation followed by rapid radiative decay, consistent with high solvent polarity and strong hydrogen bonding. In contrast, MNS in PrOH, BuOH, and PnOH exhibit rise time components with $\tau_1 = 2.9$–5.6 ps. It is a clear indication of delayed ICT formation in these less polar, and more viscous solvents. The τ_2 lifetimes increased substantially from 7.2 ps in MeOH to 60.9 ps in PrOH, and 106 ps in PnOH, reflecting prolonged emission due to reduced non-radiative decay, as seen from the lower k_{nr} values listed in Table 4. These findings indicate that in MeOH, polarity-driven stabilization leads to fast ICT dynamics and decay, while in longer-chain alcohols, viscosity governs slower ICT formation but long-lived emission due to suppressed non-radiative relaxation.

The fs-TA measurements as shown in Fig. 6 reveal complementary insight into viscosity-dependent dynamics. In all protic solvents, a pronounced ESA band around 540 nm, characteristic of the ICT state, was observed. In case of MeOH, the ESA band evolves rapidly. The global analysis reveals that the data was best fit with bi-exponential model having time components at $\tau_1 = 1.8$ ps, and $\tau_2 = 6.9$ ps. These time scales clearly indicate rapid relaxation of the ICT state. In contrast, the fs-TA spectra of MNS in PrOH, BuOH, and PnOH exhibit more persistent ESA band with an early component of $\tau_1 = 0.3$ ps, and slower component of $\tau_2 \approx 15$–17 ps, reflecting viscosity-enhanced stabilization of the ICT state. Importantly, in all these solvents, a long-lived ESA band near 600 nm emerges and it is prominent at time delays beyond 100 ps, consistent with triplet state formation. The persistence of this feature further highlights the influence of

Table 4 Kinetic parameters including the fluorescence quantum yield (Φ_{fl}), fluorescence lifetimes (τ_1 and τ_2), and the rate constants for radiative (k_r) and non-radiative (k_{nr}) decay of MNS in protic solvents. τ_1 and τ_2 were obtained from decay fitting, while relative Φ_{fl} carry an estimated uncertainty of ±5%. Uncertainties in k_r and k_{nr} were calculated by standard error propagation from Φ_{fl} and the measured lifetimes

Solvent	Φ_{fl} (10^{-2})	τ_1 (ps)	τ_2 (ps)	k_r (10^8 s^{-1})	k_{nr} (10^{10} s^{-1})
MeOH	1.2 ± 0.06	0.25 ± 0.01	7.2 ± 0.04	16.7 ± 0.84	13.7 ± 0.76
PrOH	1.6 ± 0.08	2.9 ± 0.2	60.9 ± 0.5	2.63 ± 0.13	1.62 ± 0.01
BuOH	1.7 ± 0.09	3.7 ± 0.2	66.2 ± 0.8	2.57 ± 0.14	1.48 ± 0.02
PnOH	1.8 ± 0.09	5.6 ± 0.4	106 ± 1.9	1.70 ± 0.09	0.92 ± 0.02

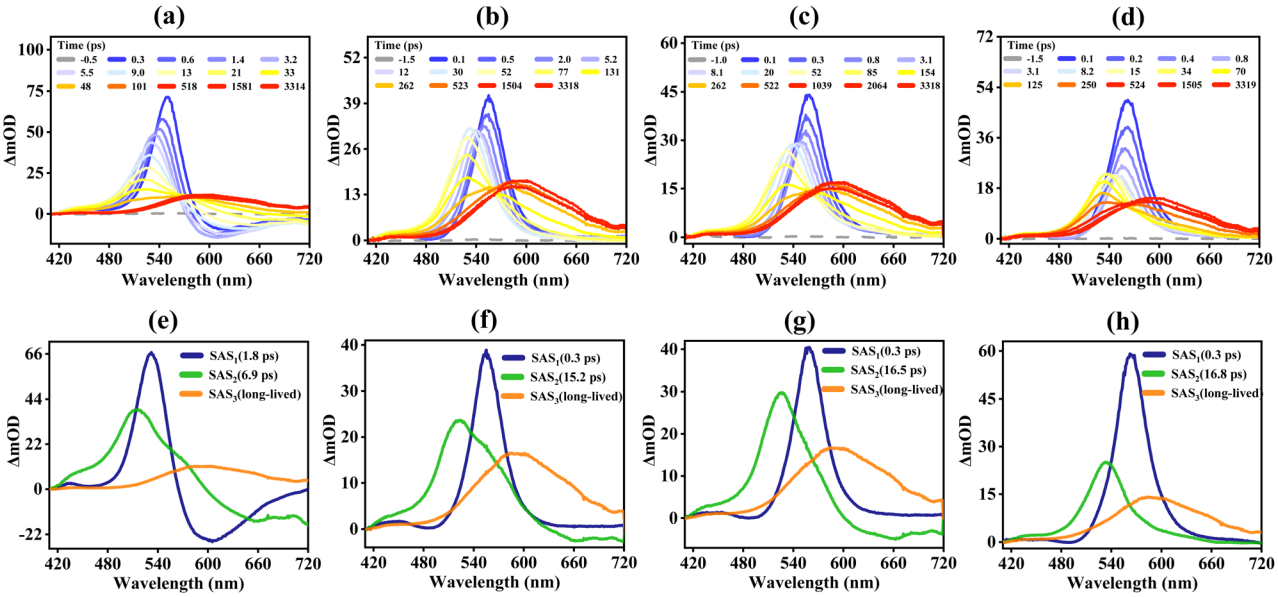

Fig. 6 The fs-TA spectra at 370 nm excitation of MNS in (a) MeOH, (b) PrOH, (c) BuOH, (d) PnOH at different time delays and (e), (f), (g), and (h) are their species-associated spectra.

restricted intramolecular motion and solvent reorganization in modulating both ICT lifetime and triplet population.

To further analyze the role of viscosity independent of hydrogen bonding, additional measurements were performed in PEG 300, a non-protic yet highly viscous solvent ($\eta \approx 80$ cP). The fluorescence upconversion measurements at 620 nm as shown in Fig. S4b exhibit a markedly extended fluorescence lifetime of 271.2 ps. It clearly indicates strong stabilization of the ICT state. Consistently, the fs-TA spectra of MNS in PEG 300 as shown in Fig. S4c showed persistent ESA features, with global analysis revealing slow decay components with $\tau_1 = 8.6$ ps, $\tau_2 = 62.4$ ps, and a long-lived ESA band near 600 nm, indicative of triplet state formation. These results confirm that high viscosity alone, even without hydrogen bonding, can significantly slow excited-state relaxation by restricting torsional and diffusive motions, thereby promoting both ICT stabilization and efficient intersystem crossing.

Computational analysis

To gain detailed insight into the excited-state behavior of MNS, TDDFT calculations were performed at the CAM-B3LYP/6-311 + G(d,p) level of theory. Both ground and excited-state geometries were optimized in MeCN, with solvent effects included using the IEFPCM. The optimized geometry maintains planarity, suggesting favourable π-conjugation across the molecule. The HOMO and LUMO are delocalized over the conjugated core, with HOMO predominantly centered on the donor unit and LUMO towards the acceptor nitro group, indicative of ICT character upon excitation as shown in Fig. 7b, and 7c. Vertical excitation energies show that S_1 (3.36 eV) and S_2 (4.00 eV), closely match with the experimental excitation wavelengths at 370 nm and 310 nm, respectively. The energy level diagram as depicted in (Fig. 8 and S5) further shows that several triplet states (T_3–T_6) lie energetically close to S_1 and S_2, enabling efficient ISC. Although excitation at 310 nm corresponds energetically to higher-lying singlet excited states, TD-DFT calculations indicate that the S_2 state in this energy region carries negligible oscillator strength (Table S1 and S2) and is therefore optically dark. Consequently, excitation at 310 nm does not selectively populate a distinct S_2 state. Instead, this excitation accesses weakly allowed higher-lying excited configurations, which undergo rapid internal conversion to the lowest singlet excited state (S_1). This interpretation is consistent with the structureless absorption profile around 310 nm and the convergence of emission and fs-TA dynamics with those observed upon direct S_1 excitation at 370 nm. To clarify the nature of the electronic

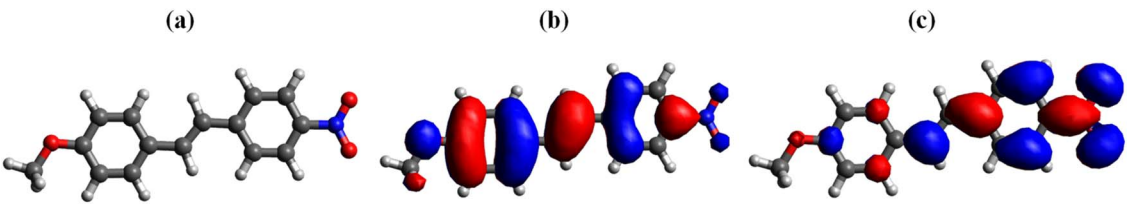

Fig. 7 (a) The optimized geometry of MNS, and its (b) HOMO and (c) LUMO electron densities.

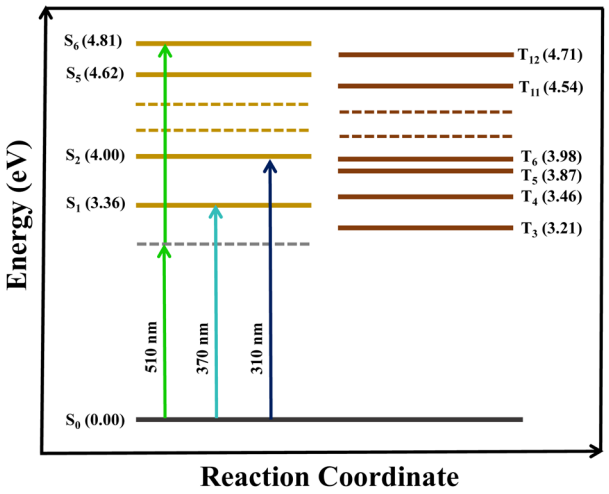

Fig. 8 Simplified energy level diagram of MNS showing the computed electronic energy levels (in eV) of key singlet and triplet states in MeCN. Experimental excitation energies (370, 310, and 510 nm) are indicated for comparison.

excitations, TD-DFT calculated excitation energies and oscillator strengths are presented as stick spectra (Fig. S6). At 510 nm, the steady-state absorption of MNS is negligible, ruling out one-photon excitation. The observed transient signals under 510 nm excitation, therefore, arise predominantly from multiphoton absorption processes. Under such conditions, population of higher-lying singlet excited-state manifolds is expected, followed by ultrafast internal conversion to lower-lying states.

SOC calculations were performed in ORCA 6.0.0 to evaluate the feasibility of ISC, and the parameters are summarized in (Tables 5 and S3). Notably, $S_1 \rightarrow T_4$ has a small energy gap ($\Delta E =$ 0.097 eV) and a large SOC constant (SOC = 8.21 cm^{-1}), suggesting a highly favourable ISC pathway. Similarly, SOC pathways are available from S_2 to T_5, T_6, and T_7, with SOC values ranging from 2.67 to 8.00 cm^{-1}, suggesting that multiple ISC channels are feasible depending on excitation energy. However, the excitation at 510 nm (2.43 eV) does not correspond to any direct one-photon transition from the ground state in the computed singlet manifold. This suggests that two-photon excitation to a CT-character S_n state may occur. Notably, the ESA profile remains centered at 540 nm without red-shift or emergence of the 600 nm band associated with triplet–triplet transition, indicating that ISC to T_4 is inefficient. This implies that 510 nm excitation accesses a distinct excited-state pathway, where relaxation remains confined within the singlet manifold or involves inefficient ISC. These findings highlight the excitation-energy dependence of relaxation dynamics in MeCN, where solvent-stabilized CT states can alter or suppress triplet state population.

NTO analysis further clarifies the nature of the involved electronic transitions (Fig. S7 and S8). The S_1 state exhibits a strong ICT character with a pronounced electron density shift from donor to acceptor regions, while T_4 represents a locally excited (LE) $\pi \rightarrow \pi^*$ state with a more confined orbital distribution. This difference in orbital character between S_1 and T_4 facilitates $S_1 \rightarrow T_4$ ISC *via* El-Sayed's rule.[59] Also, S_2 possesses a pronounced CT character, especially in its coupling with higher triplet states T_5, T_6, and T_7 as indicated by significant spatial separation in their NTOs. The consistent $\pi \rightarrow \pi^*$ nature and localized character of T_4, together with moderate SOC, support its involvement as the primary triplet state responsible for the experimentally observed long-lived ESA band at 600 nm. The computational analysis of the excited-state characteristics of MNS in TOL has also been summarized in the SI.

To further support the solvent-dependent photophysical properties of MNS, polarizability (α) and first hyperpolarizability (β) were computed in MeCN. The values of $\alpha = 4.75 \times 10^{-24}$ esu and $\beta = 2.17 \times 10^{-28}$ esu reflect enhanced electronic delocalization and a significant dipole moment change upon excitation, consistent with a stabilized ICT state in polar environments. These results compliment with the observed solvatochromic shifts and excited-state dynamics, providing additional evidence of the molecule's sensitivity to solvent polarity. Similar computational analysis in TOL was carried out and data is tabulated in Table S4. These features make MNS a promising candidate for NLO applications.

Table 5 Numerical values of SOC and singlet–triplet energy gaps (ΔE) between S_1/S_2 and triplet states (T_1–T_7) for MNS in MeCN

Triplet state	T_1	T_2	T_3	T_4	T_5
SOC (cm^{-1})	0.01	0.05	0.01	8.21	0.03
ΔE (S_1–T_n) (eV)	1.30	0.46	0.14	−0.09	−0.51
Triplet state	T_4	T_5	T_6	T_7	
SOC (cm^{-1})	0.02	8.00	3.95	2.67	
ΔE (S_2–T_n) (eV)	0.53	0.12	0.01	−0.09	

Conclusion

This study presents a comprehensive investigation of the excited-state dynamics of 4-methoxy-4′-nitrostilbene (MNS), emphasizing its sensitivity to solvent environment and excitation energy. Steady-state absorption and emission studies revealed strong intramolecular charge transfer (ICT) character, as evidenced by solvent-dependent emission shifts and increased fluorescence lifetimes in polar media. Time-resolved fluorescence measurements confirmed that both polarity and viscosity contribute to the stabilization of the ICT state and extension of its lifetime. Femtosecond transient absorption (fs-TA) studies across multiple excitation wavelengths revealed excitation-dependent relaxation behaviour. In TOL, both 370 nm and 310 nm excitations led to efficient intersystem crossing (ISC) and formation of a long-lived triplet state, evidenced by a characteristic ESA band at 600 nm. In MeCN, 370 and 310 nm excitations also resulted in triplet state formation, but with slower ISC dynamics and a weaker triplet ESA, reflecting the influence of solvent polarity on excited-state

relaxation. In contrast, 510 nm excitation in both TOL and MeCN produced a stable ESA at 540 nm that remained unchanged over time, with no spectral evolution toward the 600 nm which was associated with triplet–triplet absorption band, indicating that relaxation proceeds *via* a different pathway with inefficient ISC.

Computational studies support these experimental findings. TDDFT calculations confirmed the ICT character of S_1 and revealed energetically accessible triplet states with favourable spin–orbit coupling, enabling ISC, particularly from S_1 to T_4. The absence of a calculated one-photon transition at 510 nm aligns with the observed deviation in relaxation dynamics. Enhanced polarizability and hyperpolarizability values in polar solvents further support the influence of solvent environment on ICT stabilization.

In summary, MNS exhibits excitation and solvent-dependent excited-state dynamics, with polarity, viscosity, and excitation energy collectively modulating ICT relaxation and triplet formation. These insights emphasize the tunability of donor–acceptor chromophores and their potential in ultrafast photophysics and nonlinear optical applications.

Author contributions

Prajoy Kumar Mitra: conceptualization (equal); data curation (lead); formal analysis (lead); methodology (lead); software (lead); writing – original draft (lead); writing – review & editing (supporting). Shamil R: methodology (supporting). Yapamanu Adithya Lakshmanna: conceptualization (equal); data curation (supporting); formal analysis (lead); funding acquisition (lead); project administration (lead); supervision (lead); writing – review & editing (lead).

Conflicts of interest

The authors have no conflicts to disclose.

Data availability

Additional experimental/computational data and procedures are available in the supplementary information (SI). Supplementary information: steady-state and time-resolved absorption and fluorescence upconversion spectroscopic data, single-wavelength transient traces with fits, as well as TD-DFT analysis of UV-Vis spectra, NTO, and excitation energies, nonlinear optical parameters. See DOI: https://doi.org/10.1039/d5ra08595k.

Acknowledgements

YAL acknowledges the financial support of this work through IRG grant (ANFR/IRG/2024/001397) of ANRF. We acknowledge the computational resources provided by the Padmanabha HPC cluster at IISER TVM, India. PKM and SR acknowledge IISER TVM for the fellowship.

References

1 M. Ratner, *Nat. Nanotechnol.*, 2013, **8**, 378–381.
2 L. Mencaroni, C. Bonaccorso, V. Botti, B. Carlotti, G. Consiglio, F. Elisei, C. G. Fortuna, A. Spalletti and A. Cesaretti, *Dyes Pigm.*, 2021, **194**, 109620.
3 P. K. Samanta and R. Misra, *J. Appl. Phys.*, 2023, **133**, 020901.
4 C. Güleryüz, S. H. Sumrra, A. U. Hassan, N. K. Nkungli, M. S. Muhsan and S. M. Alshehri, *Results Chem.*, 2024, **7**, 101382.
5 S. Jasmin Finkelmeyer and M. Presselt, *Chem.–Eur. J.*, 2025, **31**, e202403500.
6 S. Li, Y. Shang, L. Wang, R. T. Kwok and B. Z. Tang, *J. Mater. Chem. C*, 2016, **4**, 5363–5369.
7 S. Ellinger, K. R. Graham, P. Shi, R. T. Farley, T. T. Steckler, R. N. Brookins, P. Taranekar, J. Mei, L. A. Padilha and T. R. Ensley, *Chem. Mater.*, 2011, **23**, 3805–3817.
8 K. Harshitha, B. Sarojini, B. Narayana, S. R. Maidur, P. S. Patil and K. Kumara, *Opt. Laser Technol.*, 2019, **117**, 304–315.
9 M. Khalid, M. U. Khan, I. Shafiq, R. Hussain, A. Ali, M. Imran, A. A. Braga, M. Fayyaz ur Rehman and M. S. Akram, *R. Soc. Open Sci.*, 2021, **8**, 210570.
10 Y. Takeda, *Acc. Chem. Res.*, 2024, **57**, 2219–2232.
11 L. Jing, P. Li, Z. Li, D. Ma and J. Hu, *Chem. Soc. Rev.*, 2025, **54**, 2054–2090.
12 V. S. Pavlovich, *ChemPhysChem*, 2012, **13**, 4081–4093.
13 Y. M. Poronik, G. V. Baryshnikov, I. Deperasińska, E. M. Espinoza, J. A. Clark, H. Ågren, D. T. Gryko and V. I. Vullev, *Commun. Chem.*, 2020, **3**, 190.
14 E. Vandaele, M. Malis and S. Luber, *J. Chem. Theory Comput.*, 2024, **20**, 3258–3272.
15 N. Puthiya Purayil, V. Kakekochi, U. K. Dalimba and C. Keloth, *ACS Appl. Electron. Mater.*, 2021, **4**, 138–148.
16 R. K. Venkatraman and A. J. Orr-Ewing, *Acc. Chem. Res.*, 2021, **54**, 4383–4394.
17 V. Farztdinov and N. Ernsting, *Chem. Phys.*, 2002, **277**, 257–270.
18 Z. Hou, Y. Huang, Y. Ruan, H. Xu, Y. Tan, L.-R. Lin and Z.-y. Wu, *RSC Adv.*, 2023, **13**, 2269–2282.
19 H. Görner and H. J. Kuhn, *Adv. Photochem.*, 1994, **19**, 1–117.
20 A. L. Dobryakov, D. Schriever, M. Quick, J. L. Pérez-Lustres, I. N. Ioffe and S. A. Kovalenko, *J. Am. Chem. Soc.*, 2024, **146**, 32463–32478.
21 M. Quick, F. Berndt, A. Dobryakov, I. Ioffe, A. Granovsky, C. Knie, R. Mahrwald, D. Lenoir, N. Ernsting and S. Kovalenko, *J. Phys. Chem. B*, 2014, **118**, 1389–1402.
22 J. S. Yang, C. K. Lin, A. M. Lahoti, C. K. Tseng, Y. H. Liu, G. H. Lee and S. M. Peng, *J. Phys. Chem. A*, 2009, **113**, 4868–4877.
23 J. S. Yang, K. L. Liau, C. M. Wang and C. Y. Hwang, *J. Am. Chem. Soc.*, 2004, **126**, 12325–12335.
24 S. Arzhantsev, K. A. Zachariasse and M. Maroncelli, *J. Phys. Chem. A*, 2006, **110**, 3454–3470.
25 K. Imato, A. Ishii, N. Kaneda, T. Hidaka, A. Sasaki, I. Imae and Y. Ooyama, *J. Am. Chem. Soc. Au*, 2023, **3**, 2458–2466.

26 D. Villarón and S. J. Wezenberg, *Angew. Chem., Int. Ed.*, 2020, **132**, 13292–13302.
27 Z. He, R. Xue, Y. Lei, L. Yu and C. Zhu, *Molecules*, 2020, **25**, 2230.
28 P. Y. Wang, Y.-C. Hsu, P. H. Chen, G. Y. Chen, Y. K. Liao and P. Y. Cheng, *Phys. Chem. Chem. Phys.*, 2024, **26**, 788–807.
29 H. Görner and D. Schultefrohlinde, *Phys. Chem.*, 1978, **82**, 1102–1107.
30 D. Schultefrohlinde and H. Görner, *Pure Appl. Chem.*, 1979, **51**, 279–297.
31 R. Mathew, S. Kayal and Y. A. Lakshmanna, *Phys. Chem. Chem. Phys.*, 2019, **21**, 22409–22419.
32 R. Mathew, P. Verma, A. Barak and Y. A. Lakshmanna, *J. Phys. Chem. A*, 2023, **127**, 7419–7428.
33 H. Gruen and H. Görner, *J. Phys. Chem.*, 1989, **93**, 7144–7152.
34 P. Roy, F. Al-Kahtani, A. N. Cammidge and S. R. Meech, *J. Phys. Chem. Lett.*, 2023, **14**, 253–259.
35 M. Haidekker, T. Brady, D. Lichlyter and E. Theodorakis, *Bioorg. Chem.*, 2005, **33**, 415–425.
36 P. K. Mitra, P. Verma and Y. A. Lakshmanna, *RSC Adv.*, 2025, **15**, 12191–12201.
37 S. Bondarev, V. Knyukshto, S. Tikhomirov, I. Kalosha, D. Bobrov, N. Masalov, N. Nevar, V. Tyvorskii, A. Kel'in and O. Kulinkovich, *J. Appl. Spectrosc.*, 2002, **69**, 230–237.
38 S. Gogoleva and V. Stsiapura, *J. Appl. Spectrosc.*, 2018, **85**, 239–245.
39 M. A. Haidekker and E. A. Theodorakis, *J. Biol. Eng.*, 2010, **4**, 11.
40 J. Kordas and M. A. El-Bayoumi, *J. Am. Chem. Soc.*, 1974, **96**, 3043–3048.
41 S. Panettieri, J. R. Silverman, R. Nifosí, G. Signore, R. Bizzarri and G. John, *ACS Omega*, 2019, **4**, 4785–4792.
42 J. Liu, C. Chen and C. Fang, *Chemosensors*, 2022, **10**, 411.
43 T. Hrivnák, M. Medveď, W. Bartkowiak and R. Zaleśny, *Molecules*, 2022, **27**, 8738.
44 C. Chen and C. Fang, *Chemosensors*, 2023, **11**, 87.
45 J. A. Sánchez-Rodríguez, A. Mohamadzade, S. Mai, B. Ashwood, M. Pollum, P. Marquetand, L. González, C. E. Crespo-Hernández and S. Ullrich, *Phys. Chem. Chem. Phys.*, 2017, **19**, 19756–19766.
46 R. R. Valiev, Y. He, T. Weltzin, A. Zhu, D. Lee, E. Moore, A. Gee, G. Drozd and T. Kurten, *Phys. Chem. Chem. Phys.*, 2025, **27**, 998–1007.
47 R. Ahmed and A. K. Manna, *J. Phys. Chem. A*, 2022, **126**, 6594–6603.
48 J. T. Buck, A. M. Boudreau, A. DeCarmine, R. W. Wilson, J. Hampsey and T. Mani, *Chem*, 2019, **5**, 138–155.
49 S. Cekli, R. W. Winkel, E. Alarousu, O. F. Mohammed and K. S. Schanze, *Chem. Sci.*, 2016, **7**, 3621–3631.
50 O. Guzman-Mendez, M. M. Reza, B. Meza, J. Jara-Cortes and J. Peon, *J. Phys. Chem. B*, 2023, **127**, 5655–5667.
51 R. Huang, J. Avó, T. Northey, E. Chaning-Pearce, P. L. Dos Santos, J. S. Ward, P. Data, M. K. Etherington, M. A. Fox and T. J. Penfold, *J. Mater. Chem. C*, 2017, **5**, 6269–6280.
52 R. Khatri and B. D. Dunietz, *J. Phys. Chem. C*, 2024, **129**, 436–446.
53 J. P. Zobel and L. González, *ChemPhotoChem*, 2019, **3**, 833–845.
54 J. P. Zobel, J. J. Nogueira and L. González, *Chem.–Eur. J.*, 2018, **24**, 5379–5387.
55 H. Görner and D. Schultefrohlinde, *J. Photochem.*, 1978, **8**, 91–102.
56 M. J. Frisch, G. W. Trucks, H. B. Schlegel, G. E. Scuseria, M. A. Robb, J. R. Cheeseman, G. Scalmani, V. Barone, G. A. Petersson, and H. Nakatsuji, *et al.*, *Gaussian 16, Revision C.01*, Gaussian, Inc., Wallingford CT, 2016.
57 F. Neese, *Wiley Interdiscip. Rev. Comput. Mol. Sci.*, 2012, **2**, 73–78.
58 W. M. Haynes, *CRC Handbook of Chemistry and Physics*, CRC press, 2016.
59 S. K. Lower and M. A. El-Sayed, *Chem. Rev.*, 1966, **66**, 199–241.